Elucidation of the Sodium – Copper Extrusion Mechanism in $CuCrS_2$: A High Capacity, Long-life Anode Material for Sodium Ion Batteries

Markus Krengel[1], Dr. Anna-Lena Hansen[1], Felix Hartmann[1], Jonas van Dinter[1] and Prof. Dr. Wolfgang Bensch[1*]

[1] Institute for Inorganic Chemistry, Christan-Albrechts-Universität zu Kiel, Max-Eyth-Str.2, 24118 Kiel, Germany

Keywords: anode material, $CuCrS_2$, sodium ion battery, ex situ X-ray diffraction, pair distribution function analysis

Abstract

The compound $CuCrS_2$ with a quasi-layered crystal structure was investigated as room temperature rechargeable sodium ion battery electrode. It exhibits an excellent performance as anode material with a high reversible capacity of 424 $mAhg^{-1}$ at 700 mAg^{-1} after 200 cycles and a capacity retention of 98.6 % compared to the third cycle. Results of *ex situ* X-Ray diffraction experiments performed at different stages of discharge demonstrate that at the beginning of Na uptake Cu^+ cations are reduced to nanosized metallic Cu particles which are expelled from the host lattice. Simultaneously Na is inserted into the host material leading to formation of $Na_{0.7}Cu_{0.15}CrS_2$ with a significantly expanded interlayer space. Metallic Cu and $Na_{0.7}Cu_{0.15}CrS_2$ coexist at this stage of discharge. Increasing the amount of Na per formula unit leads to successive conversion to X-ray amorphous Cr, nanocrystalline Na_2S and metallic Cu. The formation of highly disordered metallic Cr with domain sizes in the range of few nanometres is revealed by atomic pair distribution function analysis. During the charge process the nanocrystalline Cu particles are retained and $Na_{0.7}Cu_{0.15}CrS_2$ is at least partially reformed. The finely distributed Cu particles dramatically improve the long-time stability as evidenced by comparison of the electrochemical behaviour of mere $NaCuCrS_2$.

Introduction

Portable electronic devices, electric vehicles and stationary energy storage systems for renewable energy sources such as wind or solar power plants are increasingly utilized globally. With the increased desire of safe and low cost electrochemical energy storage systems concerns have risen, that Li resources may not be sufficient to fulfil the increased demand in the future.[1,2] Today's environmental and economical relevant topic of advanced energy storage systems for large scale application has fuelled the exploration of new potential cathode and anode materials for sodium ion batteries (SIBs).[3–6] SIBs might be a promising alternative, due to the higher availability, wider distribution and lower cost of Na compared to Li. To compete with the established Li ion technology, new electrode materials should have high specific capacities. This can be realized by utilization of conversion instead of intercalation reactions. During a conversion reaction, the electrode material is converted into new phases by Na uptake and release processes, which is accompanied by large volume changes leading to poor long time cycle stability.[7–9] To compensate this volume expansion

and to ensure a highly reversible sodiation/desodiation process with good long time stability materials with nano-scaled crystallite sizes and reduced graphene oxide (rGO) composites are primarily investigated.[10–16] In this area metal-sulfide based materials have come into the focus of research and are expected to display improved mechanical stability caused by their smaller volume change compared to metal-oxide based materials. In addition, the discharge product Na_2S has a better conductivity compared to Na_2O which is formed during the conversion of metal oxides.[4,9] Concerning layered metal-sulfide materials, MoS_2,[15,17–20] WS_2,[10,21] Sb_2S_3,[22–24] SnS_2,[12,14,25] Ni_3S_2[16,26] have been investigated as anode materials for SIBs. All these materials only showed good capacity retention and long-time cycle stability when used as rGO composite-materials, *e.g.* SnS_2-rGO showed an excellent capacity retention of about 600 mAh g^{-1} at 0.2 Ag^{-1} after 100 cycles, whereas pure SnS_2 suffered from a fast capacity fade and only delivered less than 150 mAh g^{-1} after 100 cycles applying identical conditions.[12] Until now, rGO is mostly synthesised by a modified Hummers method not suitable for application on an industrial scale.[27,28] To overcome the necessity of additives like rGO, the use of ternary, instead of binary electrode materials might be beneficial.[29,30] Applying such compounds more phases are formed during sodiation (discharge) leading to a more finely distribution of the nano-structured reaction products being in close contact. Hence short diffusion pathways are generated which are beneficial for the reversibility of the chemical reactions.[7] Copper containing chalcogenides are of special interest because during the first discharge Cu^+ cations are reduced to metallic Cu nanoparticles or dendrites by Li or Na,[31–33] increasing the electrical conductivity of the nanosized electrode materials. During our search for suitable Cu containing sulfides we identified $CuCrS_2$ as a promising candidate exhibiting a quasi-layered crystal structure. This compound has been studied concerning its structural, magnetic and thermoelectric properties,[34–40] but until now, there are no reports for the application as anode material in SIBs.

In the present study, we investigated $CuCrS_2$ as potential anode material for SIBs. Assuming a full conversion of the material with reduction of Cu^+ and Cr^{3+} to their elemental state as shown in eq. 1, the theoretical specific capacity is 597 mAh g^{-1}.

$$4\ Na^+ + CuCrS_2 + 4\ e^- \rightarrow Cu + Cr + 2\ Na_2S \quad (1)$$

The electrochemical characterizations demonstrate that the material exhibits superb capacity retention without addition of rGO. The sodiation/desodiation processes were investigated with *ex situ* XRD measurements and atomic pair distribution function (PDF) analyses evidencing the formation of a crystalline nonstoichiometric intermediate containing both Cu^+ and Na^+ followed by a complete reduction to the metal state. Herein, we report the synthesis, structural and electrochemical characterization of this promising anode material for SIBs.

Experimental

Synthesis of $CuCrS_2$

$CuCrS_2$ was synthesized via a high temperature solid-state reaction. Stoichiometric amounts of copper (Alfa Aesar, 99.9 %), chromium (chempur, 99.99%) and sulfur (Alfa Aesar, 99.999 %) were mixed and ground in a mortar. The mixture was placed in a quartz tube which was sealed under vacuum (< 10^{-4} mbar). The mixture was heated in a furnace at a heating rate of 100 K/h to 873 K, maintained at this temperature for 24 h and then annealed at 1273 K for additional 7 days. The ampoule was then slowly cooled to room temperature.

Electrochemical tests

Electrodes were prepared with 80 wt% $CuCrS_2$, 10 wt.% SUPER C65 Carbon (Timcal, Switzerland) and 10 wt.% polyvinylidene difluoride (PVdF, Solvay, Germany) suspended in NMP (N-methyl-2-pyrrolidone). The mixtures were spread on Al foil using doctor-blade casting method. Drying of the electrode foils were carried out in a vacuum oven at 60 °C for 24 h. Afterwards 10 mm discs with about 1.5 - 2 mg active material were punched out. Assembly of the Swagelok® type cells were carried out in an argon filled glovebox with water and oxygen contents below 1 ppm using Na metal as the anode, glass fibre filter disks (Whatman, United Kingdom) and Celgard® membrane as separator and a solution of 1 M $NaCF_3SO_3$ (Sigma, 98%) in diethyleneglycoldimethylether (diglyme, DGM, Sigma, 99.5 %, anhydrous) as electrolyte. Galvanostatic measurements were carried out with a Materials Mates 510 DC or a MTI 8 channel battery analyser. Cyclovoltammetric measurements were done with a Zahner XPot at a scan rate of 0.1 mVs^{-1} between 0.01 and 3 V. The lower cutoff for the first discharge was set to 0.01 V for all tested cells to ensure a full conversion.

Material characterizations

X-ray diffraction patterns (XRPD) were collected using Cu $K\alpha_1$ radiation (λ = 1.54058 Å) with a Stoe Stadi-P diffractometer equipped with a germanium monochromator and a Mythen 1K detector. Rietveld refinements [41] of the powder patterns were performed with the program FULLPROF [42] using Pseudo-Voigt function with axial divergence asymmetry to model the reflection shape and Topas Academic 6.0 [43] for extraction of microstructural details. Linear interpolation between a set of selected points was used to model the background (FullProf) and by fitting a Chebyshev polynomial (Topas Academic), respectively. Single crystal structural data were used as starting values for the lattice parameters and atomic positions ($CuCrS_2$: ICSD 24796; $NaCrS_2$: ICSD 25722, Cu: ICSD 64699, Cr: ICSD 53798, Na_2S: ICSD 60435). To account for instrumental broadening, crucial for a precise determination of microstructural characteristics, a LaB_6 standard was measured under the same conditions (NIST 660c). The size of the coherently scattering domains refer to the volume weighted average column height, calculated on the basis of the integral breadth (Voigt function model).[44] The lattice parameters *a* and *c* as well as all general atomic positions were refined. The B_{eq} values were fixed to 1 until the last step of the refinement. For *ex situ* XRD and PDF analyses, electrodes with a diameter of 2.4 cm consisting of 75 wt.% $CuCrS_2$ and 15 wt.% carbon black and 10

wt.% PVdF (Solvay, Germany) were used. The electrodes were recovered from the Swagelok® cells in an argon filled glovebox and washed with pure diglyme. After drying for 24 h in the glovebox, the material was scratched off the electrode and put in a quartz capillary with a diameter of 0.5 mm. Total scattering X-ray experiments were performed in Debye-Scherrer geometry using high energy synchrotron radiation (60 keV, λ = 0.2074 Å) at beamline P02.1 at Petra III (DESY, Hamburg). The total scattering patterns, collected with a XRD1621 PerkinElmer amorphous silicon image plate detector at a distance of 354 mm, were transformed into atomic pair distribution functions, G(r), using xPDFsuite.[45] An empty capillary was measured using identical conditions in order to subtract glass contribution to the PDF of the sample. LaB_6 (NIST 660b) was used as standard material to calibrate the instrumental contribution. Theoretical models were fit to the PDF data in the range of 1.7 to 50.0 Å with PDFgui (details in the ESI).[46]

SEM images and EDX data were obtained with a Philips ESEM XL 30 equipped with an EDAX New XL-30 detector. Acceleration voltage of 20 kV was used to detect the K-lines of the elements.

Elemental analysis (EA) was performed with a EURO VECTOR Instruments EURO EA equipped with a HEKAtech CHNS analyser.

Electron energy loss spectroscopy was carried out on a FEI Tecnai F30 STWIN microscope.

Results and Discussion

Characterization of pristine $CuCrS_2$

The compound $CuCrS_2$ crystallizes in the trigonal space group *R*3*m* and is composed of CrS_2 slabs formed by edge-sharing CrS_6 octahedra. The Cu^+ cations occupy half of the tetrahedral positions in every second layer (inset Figure 1). The structure can therefore be understood as quasi-layered, because the typical strong anisotropic nature of layered structures is observed in $CuCrS_2$. Figure 1 displays the XRD pattern of the pristine material together with the results of the Rietveld refinement. Obviously, phase pure crystalline $CuCrS_2$ was obtained and the lattice parameters were refined to a = 3.4796(4) and c = 18.691(2) Å, very close to data reported in the literature.[35]

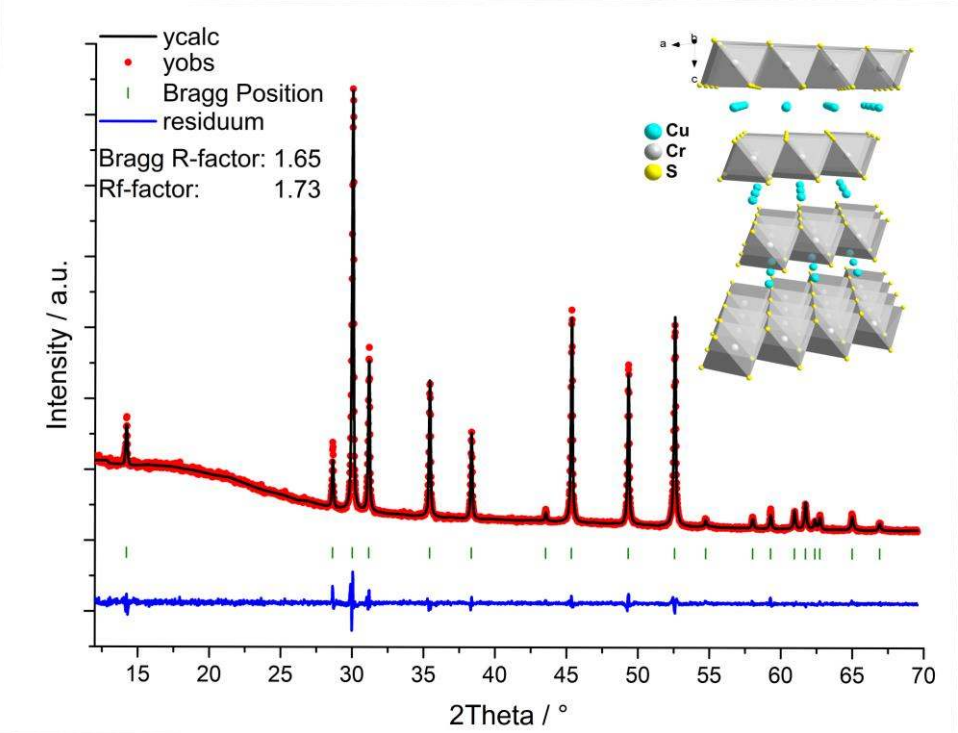

Figure 1. Rietveld refinement results of the XRD pattern of $CuCrS_2$. Observed (red circles), calculated (black line) and difference (blue line) profiles. Bragg reflection positions are marked as vertical bars. The inset shows the crystal structure.

The combined results from EDX measurements and EA (Figure S1, Table S1 and S2) reveal a composition of $Cu_{0.99(1)}Cr_{0.98(1)}S_{2.03(1)}$ in agreement with the desired stoichiometry. SEM images show a broad size distribution of the particles, which is typical for products of solid-state reactions, and the layered nature of the material is clearly visible (Figure S2).

Electrochemical characterization

In several publications it was reported that ether-based electrolytes show a superior cycle life in LIBs and SIBs containing sulfide based materials, and therefore $NaCF_3SO_3$ in DGM was chosen here.[47–49] In order to improve the cycling stability, different cut-off potentials were applied at a current density of 120 mAg^{-1} for the first and 600 mAg^{-1} for subsequent cycles (Figure 2). When cycled in the voltage range of 3 - 0.01 V, the capacity fades slowly from 520 to 445 $mAhg^{-1}$ from the third to the 70th cycle and followed by a quick capacity drop for subsequent cycles down to 121 $mAhg^{-1}$ at cycle 100 (Figure 2a).

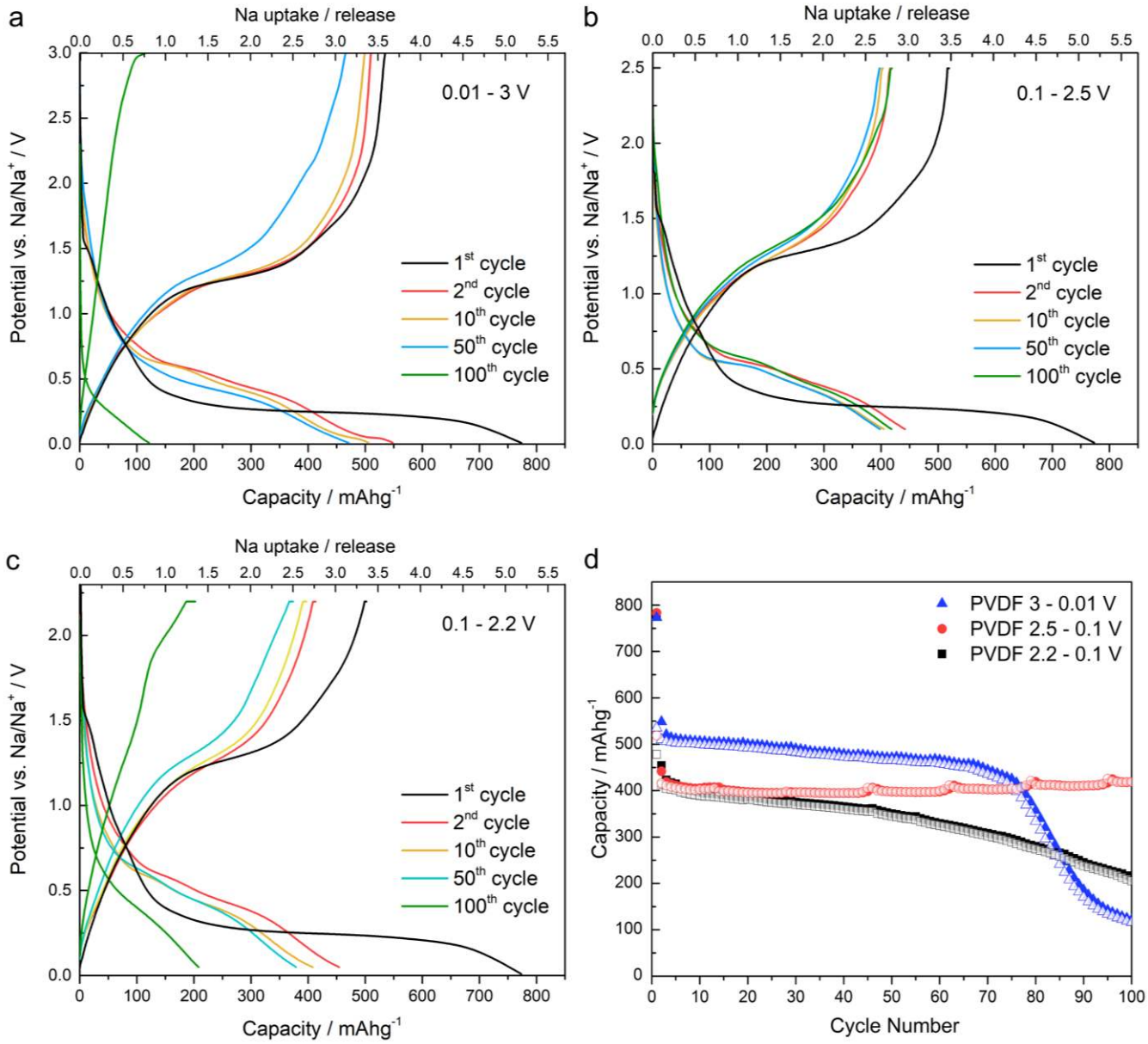

Figure 2. Performance of Na/$CuCrS_2$ test cells applying different potential windows. Discharge-charge profiles at a current dencity of 120 mAg^{-1} for the first and 600 mAg^{-1} for subsequent cycles, cycled between (a) 0.01 and 3 V, (b) 0.1 and 2.5 V and (c) 0.1 and 2.2 V. CCCV charge mode was applied (end current 50 % of the initial current). (d) Discharge (filled) and charge (hollow) capacities at different cut-off voltages.

Discharging to voltages below 0.1 V leads to electrolyte destruction visible in the CV curves (Figure S3) and resulting in low Coulombic efficiencies (< 98 %), causing the fast drop in capacity after 70 cycles because the test cells got dry. When limiting the cut-off voltages to 0.1 V and 2.2 V a slow but steady loss in capacity from 423 $mAhg^{-1}$ (corresponding to 2.83 Na/$CuCrS_2$) at the third to 212 $mAhg^{-1}$ (corresponding to 1.42 Na/$CuCrS_2$) at the 100th cycle can be observed, indicating that the desodiation process is not finished at 2.2 V (Figure 2c). When the upper cut-off voltage is set to 2.5 V the cell exhibits excellent capacity retention of about 420 $mAhg^{-1}$ (corresponding to 2.81 Na/$CuCrS_2$) during the first 100 cycles. Figure 2b displays a selection of galvanic discharge/charge profiles of the $CuCrS_2$ cell with cut-off voltages of 0.1 and 2.5 V from the second cycle. The initial discharge occurs stepwise, with a fast decrease of the open circuit voltage at the beginning followed by a first small pseudo-

plateau at 1.5 V. The second step is seen in the voltage range of about 0.9 to 0.4 V and is barely noticeable in the galvanostatic measurement but clearly visible in CV profile (Figure S3). At 0.4 V a well pronounced plateau can be observed. After the uptake of 4.2 Na/$CuCrS_2$ the voltage steadily decreases until the cut-off of 0.01 V is reached and an initial capacity of 773 $mAhg^{-1}$ was achieved. During the first charge a constant voltage gain up to 1.2 V (1 Na released) is followed by a pseudo-plateau in the range of 1.2 to 1.5 V (2.8 Na released). Upon further Na release the voltage raises with increasing slope until the cut-off potential of 2.5 V, leading to a initial charge capacity of 519 $mAhg^{-1}$ (3.5 Na released). The subsequent cycles show a highly reverable process involving the cycling of about 2.7 Na per formula unit. The irreversible capacity loss is 254 $mAhg^{-1}$, corresponding to an efficiency of 67 % in the frist cycle. From the third cycle an Coulombic efficiency >99 % is achieved. Figure 2d displays a comparison of the accieved discharge capacity for the different cut-off potentials.

Investigation of structural changes occurring during the discharge/charge processes

To investigate the processes taking place during sodiation and desodiation *ex situ* XRD measurements have been performed (Figure 3). During uptake of 1 Na per formula unit the reduction of Cu^+ to metallic Cu is evidenced by the appearance of the (111) and (200) reflections of Cu (Figure 3a, orange trace B). Rietveld refinement revealed a pronounced (111) texture, caused by a preferred growth direction of Cu crystallites. A new phase is formed with the reflection positions matching nearly with those of $NaCrS_2$ as can be seen comparing the calculated pattern (red) with the pattern B (orange) in Figure 3a.

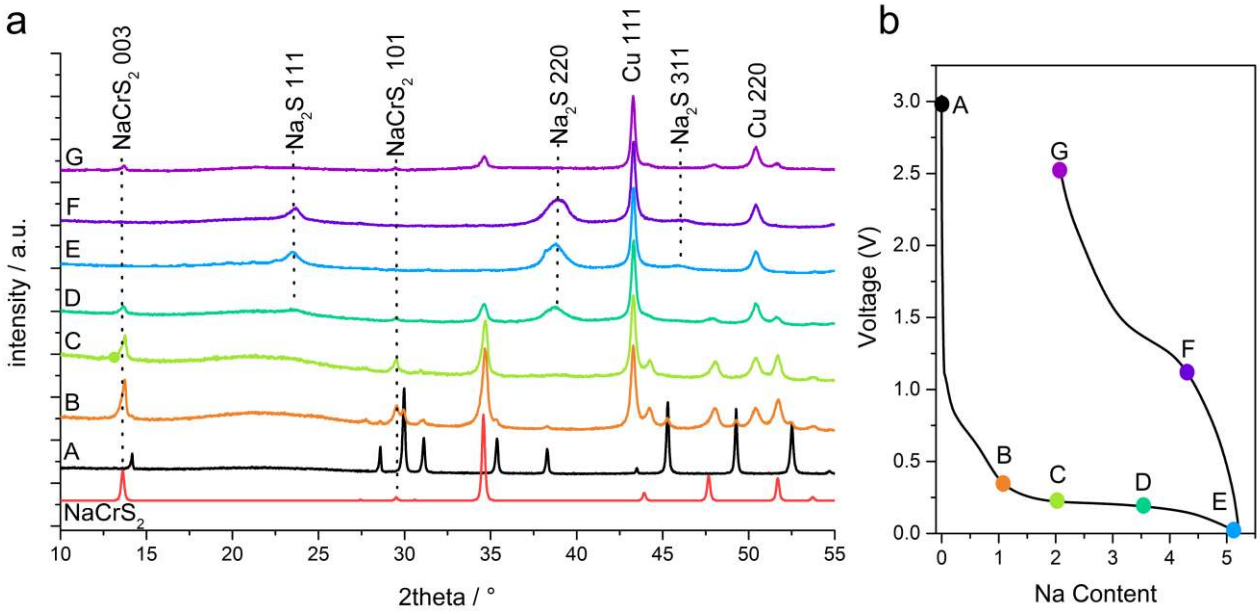

Figure 3. *Ex situ* XRD patterns of the $CuCrS_2$ electrode collected at various points (a), as indicated in the corresponding discharge-charge profile (b).

But the analysis of the relative intensities of the Bragg reflections showed a notable deviation of the (003)/(101) intensity ratio expected for $NaCrS_2$. Rietveld refinement clearly unveiled the presence of about 15% Cu still occupying the tetrahedral position (0, 0, 0.152), resulting in a non-stoichiometric

compound with composition $Na_{0.70(3)}Cu_{0.15(3)}CrS_2$. No evidence was found that either the Cr or the S atomic positions deviate from full occupancy. According to these results 15% of cation vacancies must be present in the structure. Additionally, weak reflections of $CuCrS_2$ are still visible, and phase fraction refinement yields about 8 wt% for $CuCrS_2$, 69 wt% for $Na_{0.70(3)}Cu_{0.15(3)}CrS_2$ and 23 wt% for elemental Cu. The remaining $CuCrS_2$ and the loss of Na can be explained by the consumption of Na to form the SEI layer. The lattice parameters of $Na_{0.70(3)}Cu_{0.15(3)}CrS_2$ (a = 3.5306(1) and c = 19.262(1) Å, Table S3) demonstrate a significant expansion of the interlayer space caused by the larger radius of Na^+ compared to that of Cu^+. The reflections of all three components are broadened and the coherently scattering domains are in the nano-regime (Table S3).

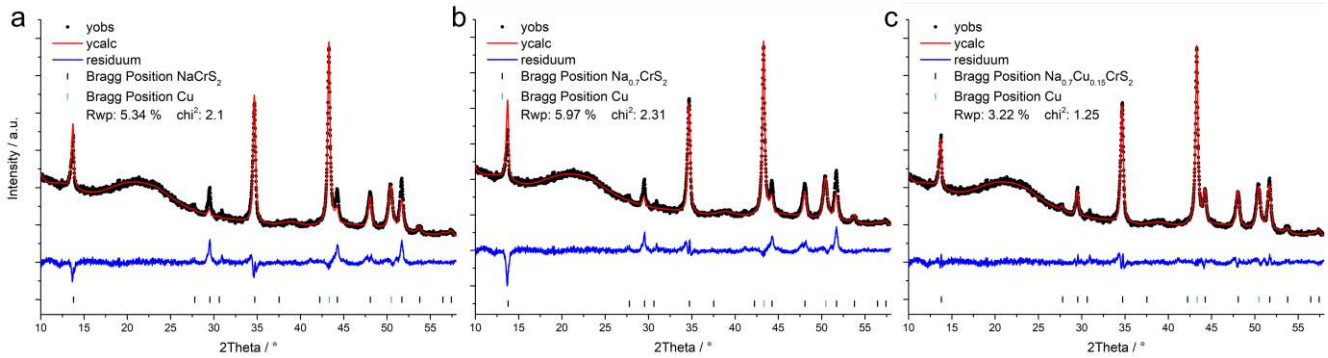

Figure 4. Rietveld refinement results of the XRD pattern after the uptake of 2 Na. Observed (black circles), calculated (red line) and difference (blue line) profiles. Bragg reflection positions are marked as vertical black bars for (a) $NaCrS_2$, (b) $Na_{0.7}CrS_2$ and (c) $Na_{0.7}Cu_{0.15}CrS_2$ and green for copper.

After uptake of 2 Na per formula unit the remaining weak reflections of $CuCrS_2$ vanished and only the (001) reflection of $CuCrS_2$ with a very low intensity is visible. (Figure 3a, pattern C). The results of the Rietveld refinements assuming the different chemical compositions $NaCrS_2$, $Na_{0.7}CrS_2$ or $Na_{0.7}Cu_{0.15}CrS_2$ and Cu after uptake of 2 Na are displayed in Figure 4. Only for $Na_{0.7}Cu_{0.15}CrS_2$ a satisfactory refinement could be achieved giving the lowest value for χ^2 of 1.25 and a R_{wp} value of 3.22% (Rietveld profiles for 1 and 3.5 Na uptake are displayed in the ESI Figure S5). This result is in line with the refined lattice parameters which are virtually identical with those obtained for the Na containing sample after uptake of 1 Na per formula unit (Table S3). In addition, the amount of Cu in the sample increased to ca. 30 wt%, while the content of $Na_{0.7}Cu_{0.15}CrS_2$ decreased to about 54 wt%. An additional weak and broad reflection located at ca. 38° 2θ (a magnification is shown in Figure S4) can be assigned to Na_2S with coherently scattering domain sizes of only about ~ 2 nm. At this point of Na uptake, the intensity ratio of the $Na_{0.7}Cu_{0.15}CrS_2$ to Cu reflection has decreased, indicating the beginning of conversion of $Na_{0.7}Cu_{0.15}CrS_2$ into an X-ray amorphous state and Na_2S, accompanied by a reduction of the domain size of the $Na_{0.7}Cu_{0.15}CrS_2$ phase from about 65 to about 33 nm (Table S3). During further Na uptake the intensity of reflections of the intermediate $Na_{0.7}Cu_{0.15}CrS_2$ decreases and Na_2S with a volume weighted averaged domain size of ~ 6 nm becomes clearly visible (pattern D in Figure 3a, point D in 3b). At the fully discharged stage (pattern E in Figure 3a, point E in 3b) only reflections of Cu and Na_2S are visible. We note that no reflections of elemental Cr can be identified suggesting that the particles are too small to be detected in the XRD patterns due to the lack of long-

range order. We note that this is a common observation for conversion reactions of materials: for Cu containing compounds the formation of nanocrystalline Cu particles was reported, while for other transitions metal containing samples the metal cations are converted into an X-ray amorphous state. [8,31,49–55]

Weak but clearly visible reflections of $Na_{0.7}Cu_{0.15}CrS_2$ appear again after the first charge (point G in Figure 3), confirming that during the first cycle not all Cu^+ ions could be replaced, as indicated by Rietveld refinement. The formation of an at least partially crystalline phase is quiet astonishing, because in the overwhelming cases a formation of a crystalline phase during charge after a full conversion is not observed.

As a consequence to absent extractable information on the nature of chromium in the fully discharged state using XRD, *ex situ* total scattering experiments were performed to calculate the corresponding PDF of a sample after the first (Figure 5) and second cycle (Figure S7). A real space model based on nano crystalline Na_2S and Cu matches well in the mid-range of 20 - 50 Å (Figure S7), but pronounced deviations are obvious in the short-range region (< 10 Å). This discrepancy indicates an insufficient modelling of experimental data applying only these two constituents. A comparison of the difference curve (blue line, Figure 5) with a modelled PDF of 2 nm chromium particles displays good agreement of the major features of the idealized Cr PDF and the residue (green dotted line in Figure 5). Consequently, these features can be attributed to Cr-Cr bonds, especially recognisable in the first and second coordination shell of an ideal bcc Cr structure being 2.5 Å and 2.9 Å, receptively. An attempt to include Cr into the model and fit it to the calculated PDF in a Rietveld like least-squares approach, led to an improved R_{wp} value of 10.3 %, but resulted in physically unsound atomic displacement factors or very small particle sizes (Table S4 and Figure S7 b). These abnormalities indicate the presence of highly disordered nanoparticles, *e.g.* a high abundance of stacking faults.[56] Comparable results were obtained for a sample after full discharge in the second cycle, the PDFs being nearly superimposable (Figure S8), indicating the successive conversion to nano-scaled Cu, Cr and Na_2S to be a highly reversible process during cycling.

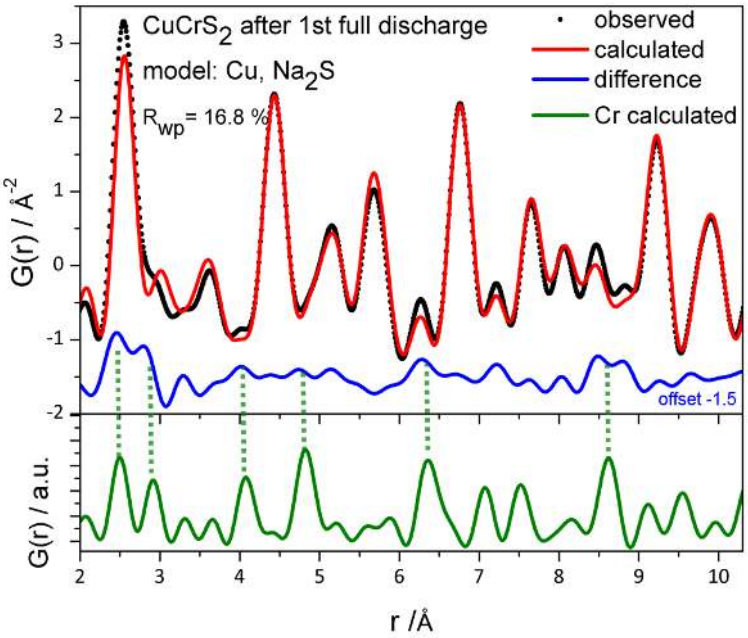

Figure 5. Atomic pair distribution function analysis of $CuCrS_2$ after the uptake of 5 Na with a model including only Cu and Na_2S. The difference curve in is compared to a model for Cr (D_m = 2 nm), as indicated by green dashed lines.

Considering the results of the investigations, we assume the following reactions for the first discharge (eq. 2a, b). The first step is the irreversible cation exchange mechanism of Cu^+ and Na^+ with simultaneous reduction of Cu^+ to metallic Cu, followed by the reversible full conversion of the intermediate phase $Na_{0.7}Cu_{0.15}CrS_2$ to Cr and Na_2S. During charge elemental Cr and Na_2S react and $Na_{0.7}Cu_{0.15}CrS_2$ is partially reformed, while parts of Cu remais in the elemental state according to eq 2b.

$$0.7\ Na^+ + CuCrS_2 + 0.7\ e^- \rightarrow 0.85\ Cu + Na_{0.7}Cu_{0.15}CrS_2 \quad (2a)$$

$$3.3\ Na^+ + 0.85\ Cu + Na_{0.7}Cu_{0.15}CrS_2 + 3.3\ e^- \leftrightarrow Cu + Cr + 2\ Na_2S \quad (2b)$$

According to eq. 2a and 2b $CuCrS_2$ can deliver a reversible capacity of 492 $mAhg^{-1}$ which is in good agreement with the measured values at lower current densities of 400 mAg^{-1} (Figure 2). To evaluate the role of metallic Cu formed upon first discharge of $CuCrS_2$, we also used pure $NaCrS_2$ (Figure S9; active material: ca. 1.5 mg, details in the ESI) applying PVdF as binder. Appling the same discharge/charge conditions the performance of the $NaCrS_2$ electrode is far inferior compared to $CuCrS_2$: at 200 mAg^{-1} the capacity drops within few cycles and cycling stability is significantly lower than for $CuCrS_2$. Even at lower current densities and a wider potential range the $NaCrS_2$ electrodes suffer from poor capacity retention (Figure S10). For this cell the capacity quickly faded within the first 20 cycles even at low current densities of 200 mAg^{-1} and only 100 mAh g^{-1} were obtained after 100 cycles as shown in Figure S10. This supports our assumption that nanocrystalline Cu has a beneficial effect enhancing the electrochemical properties of the electrode by compensating the poor electrical conductivity of $NaCrS_2$ ($\rho = 10^5\ \Omega\cdot cm$).[57]

Investigation of cycling stability and rate performance

The rate performance of $CuCrS_2$ (PVdF as binder) is shown in Figure 6a. The cell delivered a reversible capacity of 450, 415, 326, 240 and 158 $mAhg^{-1}$ for current densities of 400, 600, 1000, 1500 and 2000 mAg^{-1}, respectively. When the current density is reset to 400 mAg^{-1}, a capacity of 448 $mAhg^{-1}$ could be recovered. This high rate-stability is remarkable for a non-rGO composite conversion material with electrodes containing only 10 wt% carbon black and binder. The superior rate capability become clear when compared to other pure layered metal sulfides. SnS_2 delivered a capacity of about 550 $mAhg^{-1}$ at 30 mAg^{-1} dropping to less than 100 $mAhg^{-1}$ when applying a current density of 810 mAg^{-1}.[58] For pure MoS_2 capacities of about 390 $mAhg^{-1}$ at 40 $mAgh^{-1}$ and about 200 $mAhg^{-1}$ at 640 mAh^{-1} have been reported. But here, the capacity did not recover when the current density was reversed to 40 mAg^{-1}.[59] Even the composite WS_2@graphene delivered just 380 $mAhg^{-1}$ at 40 mAg^{-1} but only 110 $mAhg^{-1}$ at a current density of 640 mAg^{-1}.[21]

The cycling performance of the $CuCrS_2$ electrodes at different current rates is presented in Figure 6b. At a current rate of 700 mAg^{-1} a capacity of 430 $mAhg^{-1}$ (corresponding to 2.88 Na/$CuCrS_2$) was reached at the third cycle remaining nearly constant for 200 cycles. At cycle 200, a capacity of 424 $mAhg^{-1}$ was achieved (corresponding to 2.84 Na/$CuCrS_2$) leading to a capacity retention of 98.6 % compared with cycle three. At a current density of 1500 mAg^{-1} the capacity drops slightly from the second cycle (310 $mAhg^{-1}$, 2.01 Na) to 254 $mAhg^{-1}$ within the first 50 cycles, remaining constant at this level. A capacity of 252 $mAhg^{-1}$ was achieved at cycle 500. These results evidence the excellent long-time stability of the $CuCrS_2$ electrodes.

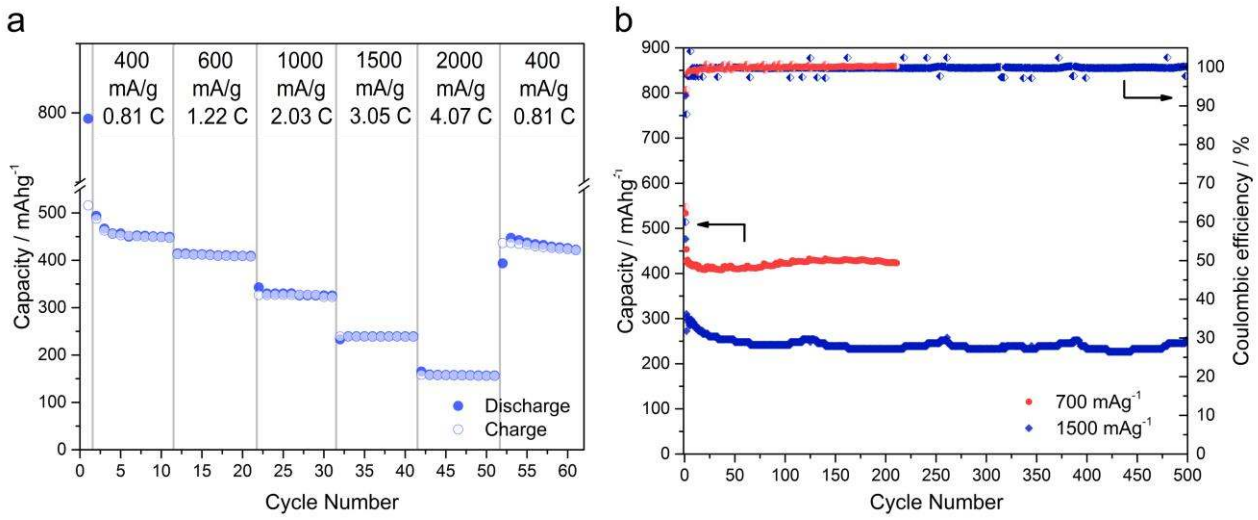

Figure 6. (a) Rate capability at various current densities from 0.4 to 2 Ag^{-1}. (b) Cycling performance and charge efficiency of $CuCrS_2$ cells, using galvanostatic cycling at 0.7 and 1.5 Ag^{-1}in the range of 0.1 – 2.5 V. Average values of two identical cells are displayed. (C rates are based on the theoretical reversable capacity of 492 $mAhg^{-1}$)

Conclusions

We demonstrated that $CuCrS_2$ is an excellent anode material for sodium ion storage. A superior high and stable capacity of 424 $mAhg^{-1}$ is achieved at high C rates in the 200th cycle. The evolution of nanocrystalline metallic Cu particles during the first discharge leads to an improved electron transport, which explains the superior rate stability compared to other pure transition metal sulfides. *Ex situ* XRD analyses elucidated a successive conversion of $CuCrS_2$ to Cu and the intermediate phase $Na_{0.7}Cu_{0.15}CrS_2$, followed by a full conversion. The formation of Na_2S and metallic Cu could be clearly demonstrated by *ex situ* XRD measurements, while PDF analysis unveiled the presence of nano-scaled, most probably highly disordered metallic Cr in the discharged state. During the charge process Na_2S disappears while nanocrystalline Cu is still present and $Na_{0.7}Cu_{0.15}CrS_2$ is reformed. These results underline that ternary compounds might be superior compared to mere binary compounds in terms of rate and long-time cycle stability.

Acknowledgments

We kindly thank Prof. Lorenz Kienle and Julian Strobel for electron energy loss spectroscopy measurements. Financial support by the State of Schleswig-Holstein is acknowledged. The authors thank the German Electron Synchrotron (DESY) and Huayna Terraschke for beamtime allocation.

Conflict of Interest

The authors declare no conflict of interest.

Keywords: sodium ion battery; reaction mechanism; pair distribution function analysis; Rietveld refinements; conversion

Supporting Information

SEM / EDX measurements; results of the elemental analysis; additional *ex situ* XRD powder patterns; cyclovoltammetric measurement; results of Rietveld refinement for different sodium contents, additional PDF analysis

References

[1] N. L. Panwar, S. C. Kaushik, S. Kothari, *Renewable Sustainable Energy Rev.* **2011**, *15*, 1513–1524.

[2] D. Larcher, J.-M. Tarascon, *Nat. Chem.* **2014**, *7*, 19–29.

[3] J.-Y. Hwang, S.-T. Myung, Y.-K. Sun, *Chem. Soc. Rev.* **2017**, *46*, 3529–3614.

[4] Y. Xiao, S. H. Lee, Y.-K. Sun, *Adv. Energy Mater.* **2017**, *7*, 1601329.

[5] L. Shi, T. Zhao, *J. Mater. Chem. A* **2017**, *5*, 3735–3758.

[6] F. Wang, X. Wu, C. Li, Y. Zhu, L. Fu, Y. Wu, X. Liu, *Energy Environ. Sci.* **2016**, *9*, 3570–3611.

[7] P. K. Nayak, L. Yang, W. Brehm, P. Adelhelm, *Angew. Chem. Int. Ed.* **2017**.

[8] F. Klein, B. Jache, A. Bhide, P. Adelhelm, *Phys. Chem. Chem. Phys.* **2013**, *15*, 15876.

[9] M. Sawicki, L. L. Shaw, *RSC Adv.* **2015**, *5*, 53129–53154.

[10] S. H. Choi, Y. C. Kang, *Nanoscale* **2015**, *7*, 3965–3970.

[11] Y. Du, X. Zhu, X. Zhou, L. Hu, Z. Dai, J. Bao, *J. Mater. Chem. A* **2015**, *3*, 6787–6791.

[12] B. Qu, C. Ma, G. Ji, C. Xu, J. Xu, Y. S. Meng, T. Wang, J. Y. Lee, *Adv. Mater.* **2014**, *26*, 3854–3859.

[13] S. H. Choi, Y. C. Kang, *Nanoscale* **2015**, *7*, 6230–6237.

[14] Y. C. Lu, C. Ma, J. Alvarado, N. Dimov, Y. S. Meng, S. Okada, *J. Mater. Chem. A* **2015**, *3*, 16971–16977.

[15] X. Xu, D. Yu, H. Zhou, L. Zhang, C. Xiao, C. Guo, S. Guo, S. Ding, *J. Mater. Chem. A* **2016**, *4*, 4375–4379.

[16] W. Qin, T. Chen, T. Lu, D. H. C. Chua, L. Pan, *J. Power Sources* **2016**, *302*, 202–209.

[17] L. David, R. Bhandavat, G. Singh, *ACS Nano* **2014**, *8*, 1759–1770.

[18] J. Park, J.-S. Kim, J.-W. Park, T.-H. Nam, K.-W. Kim, J.-H. Ahn, G. Wang, H.-J. Ahn, *Electrochim. Acta* **2013**, *92*, 427–432.

[19] C. Zhu, X. Mu, P. A. van Aken, Y. Yu, J. Maier, *Angew. Chem.* **2014**, *126*, 2184–2188.

[20] T. S. Sahu, Q. Li, J. Wu, V. P. Dravid, S. Mitra, *J. Mater. Chem. A* **2017**, *5*, 355–363.

[21] D. Su, S. Dou, G. Wang, *Chem. Commun.* **2014**, *50*, 4192.

[22] D. Y. W. Yu, P. V. Prikhodchenko, C. W. Mason, S. K. Batabyal, J. Gun, S. Sladkevich, A. G. Medvedev, O. Lev, *Nat. Commun.* **2013**, *4*, DOI 10.1038/ncomms3922.

[23] Y. Zhu, P. Nie, L. Shen, S. Dong, Q. Sheng, H. Li, H. Luo, X. Zhang, *Nanoscale* **2015**, *7*, 3309–3315.

[24] S. M. Hwang, J. Kim, Y. Kim, Y. Kim, *J. Mater. Chem. A***2016**, *4*, 17946–17951.

[25] W. Sun, X. Rui, D. Yang, Z. Sun, B. Li, W. Zhang, Y. Zong, S. Madhavi, S. Dou, Q. Yan, *ACS Nano* **2015**, *9*, 11371–11381.

[26] J.-S. Kim, H.-J. Ahn, H.-S. Ryu, D.-J. Kim, G.-B. Cho, K.-W. Kim, T.-H. Nam, J. H. Ahn, *J. Power Sources* **2008**, *178*, 852–856.

[27] W. S. Hummers Jr, R. E. Offeman, *J. Am. Chem. Soc.* **1958**, *80*, 1339–1339.

[28] R. Raccichini, A. Varzi, S. Passerini, B. Scrosati, *Nat. Mater.* **2014**, *14*, 271–279.

[29] M. Krengel, P. Adelhelm, F. Klein, W. Bensch, *Chem. Commun.* **2015**, *51*, 13500–13503.

[30] X. Y. Yu, X. W. David Lou, *Adv. Energy Mater.* **2018**, *8*, 1701592.

[31] V. Bodenez, L. Dupont, L. Laffont, A. R. Armstrong, K. M. Shaju, P. G. Bruce, J.-M. Tarascon, *J. Mater. Chem.* **2007**, *17*, 3238.

[32] V. Bodenez, L. Dupont, M. Morcrette, C. Surcin, D. W. Murphy, J.-M. Tarascon, *Chem. Mater.* **2006**, *18*, 4278–4287.

[33] W. Bensch, J. Ophey, H. Hain, H. Gesswein, D. Chen, R. Mönig, P. A. Gruber, S. Indris, *Phys. Chem. Chem. Phys.* **2012**, *14*, 7509.

[34] N. Le Nagard, G. Collin, O. Gorochov, *Mater. Res. Bull.* **1979**, *14*, 1411–1417.

[35] P. F. Bongers, C. F. Van Bruggen, J. Koopstra, W. P. F. A. M. Omloo, G. A. Wiegers, F. Jellinek, *J. Phys. Chem. Solids* **1968**, *29*, 977–984.

[36] G. M. Abramova, A. M. Vorotynov, G. A. Petrakovskii, N. I. Kiselev, D. A. Velikanov, A. F. Bovina, R. F. Al'mukhametov, R. A. Yakshibaev, É. Gabitov, *Phys. Solid State* **2004**, *46*, 2225–2228.

[37] G. C. Tewari, T. S. Tripathi, A. K. Rastogi, *J. Electron. Mater.* **2010**, *39*, 1133–1139.

[38] D. Srivastava, G. C. Tewari, M. Karppinen, R. M. Nieminen, *J. Phys.: Condens. Matter* **2013**, *25*, 105504.

[39] D. Srivastava, G. C. Tewari, M. Karppinen, *J. Phys.: Condens. Matter* **2014**, *26*, 505501.

[40] A.-L. Hansen, T. Dankwort, H. Groß, M. Etter, J. König, V. Duppel, L. Kienle, W. Bensch, *J. Mater. Chem. C* **2017**,*5*, 9331-9338.

[41] H. M. Rietveld, *J. Appl. Crystallogr.* **1969**, *2*, 65–71.

[42] J. Rodríguez-Carvajal, *Phys. B Condens. Matter* **1993**, *192*, 55–69.

[43] *Topas Academic 6.0*, Coelho Software, Australia, **2016**.

[44] D. Balzar, Voigt-function model in diffraction linebroadening analysis, defects and microstructure: Analysis by diffraction, (Eds.: R. L. Snyder, H. J. Bunge, J. Fiala), Oxford University Press, New York, **1999,** pp 94-124.

[45] X. Yang, P. Juhas, C. L. Farrow, S. J. L. Billinge, *ArXiv14023163 Cond-Mat* **2014**.

[46] C. L. Farrow, P. Juhas, J. W. Liu, D. Bryndin, E. S. Božin, J. Bloch, T. Proffen, S. J. L. Billinge, *J. Phys.: Condens. Matter* **2007**, *19*, 335219.

[47] Y. Fu, A. Manthiram, *Electrochim. Acta* **2013**, *109*, 716–719.

[48] Y. Zhu, L. Suo, T. Gao, X. Fan, F. Han, C. Wang, *Electrochem. Commun.* **2015**, *54*, 18–22.

[49] M. Krengel, A.-L. Hansen, M. Kaus, S. Indris, N. Wolff, L. Kienle, D. Westfal, W. Bensch, *ACS Appl. Mater. Interfaces* **2017**, *9*, 21283–21291.

[50] M. Walter, T. Zünd, M. V. Kovalenko, *Nanoscale* **2015**, *7*, 9158–9163.

[51] X. Ou, X. Liang, F. Zheng, Q. Pan, J. Zhou, X. Xiong, C. Yang, R. Hu, M. Liu, *Chem. Eng. J.* **2017**, *320*, 485–493.

[52] C. Yang, X. Ou, X. Xiong, F. Zheng, R. Hu, Y. Chen, M. Liu, K. Huang, *Energy Environ. Sci.* **2017**, *10*, 107–113.

[53] R. Verma, K. R, U. V. Varadaraju, *Appl. Surf. Sci.* **2017**, *418*, 30–39.

[54] R. Verma, R. K. Raman, U. V. Varadaraju, *J. Solid State Electrochem.* **2016**, *20*, 1501–1505.

[55] H. Li, Y. Wang, J. Jiang, Y. Zhang, Y. Peng, J. Zhao, *Electrochim. Acta* **2017**, *247*, 851–859.

[56] A. S. Masadeh, E. S. Božin, C. L. Farrow, G. Paglia, P. Juhas, S. J. L. Billinge, A. Karkamkar, M. G. Kanatzidis, Phys. Rev. B **2007**, *76*, 115413.

[57] R. V. Moshtev, *J. Electrochem. Soc.* **1981**, *128*, 1399.

[58] T. Zhou, W. K. Pang, C. Zhang, J. Yang, Z. Chen, H. K. Liu, Z. Guo, *ACS Nano* **2014**, *8*, 8323–8333.

[59] X. Xie, Z. Ao, D. Su, J. Zhang, G. Wang, *Adv. Funct. Mater.* **2015**, *25*, 1393–1403.

TOC

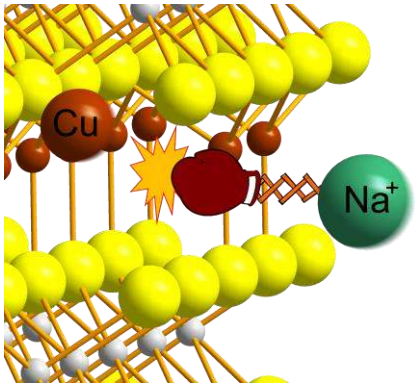

Get out of my way: The sodium – copper extrusion mechanism of $CuCrS_2$ was studied using *ex situ* XRD measurements, Rietveld refinements and PDF analysis. $CuCrS_2$ exhibits a very complex phase transition in the early stage of Na uptake to form $Na_{0.70}Cu_{0.15}CrS_2$ followed by the full conversion to Cu, Cr and Na_2S. This reaction is highly reversible leading to a capacity of 424 $mAhg^{-1}$ after the 200th cycle.